Chapter 6

Band splitting-driven Berry curvature and sign reversal of anomalous Hall effect in the manganese pnictide MnSb

This chapter provides evidence of the change in sign and magnitude of intrinsic anomalous Hall conductivity in the MnSb compound, which may arise due to the anisotropic electronic band structure around the spin reorientation transition (SRT). In addition, we observed the THE due to the emergence of skyrmionic bubbles below the SRT, whereas above the SRT, the giant value of THE might be attributed to the microscopic non-coplanar magnetic texture.

6.1 Introduction

Mn-based pnictides with formula MnX (X = N, P, As, Sb) and NiAs-type hexagonal structure, exhibit exotic functional properties such as unique electronic band structure, elastic properties and mechanism of superconductivity under high pressure [1]. The Mn pnictides have gained renewed recognition in high-temperature spintronics research due to their peculiar band structure, high Curie temperature, spin reorientation transition, and large uniaxial magneto-crystalline anisotropy (MCA) [2, 3, 4, 5, 6, 7, 8, 9, 10]. Recently, extensive research has been carried out to unravel the sign reversal of AHE due to many factors such as spin orientation [11, 12, 13, 14], the value of magnetization [15] and the interface induced SOC or breaking inversion symmetry [16], nevertheless, further research is still needed in various compounds to establish a clear picture [17]. A most recent study on the MnAs compound has been demonstrated the SOC-induced band splitting and enhanced intrinsic AHC depending on the magnetization orientation [18, 19]. In a similar Mn pnictide, MnBi, the topological Hall effect (THE) has also been discovered due to the microscopic non-coplanar spin structure and the mesoscopic topological skyrmionic bubble, resulting from the uniaxial MCA [9]. This observation inspired us to explore other Mn pnictides. A neutron diffraction study [8] and a recent magneto-transport study [5] in a composition close to MnSb indicates the presence of spin reorientation transition (SRT) and AHE, respectively. To explore the effect of SRT on the electronic band structure and the AHE, and to search for the THE, we performed a detailed experimental and theoretical investigation of AHE and THE in a pure stoichiometric MnSb compound with a large uniaxial MCA.

In this work, we present a comprehensive study of the AHE and THE in the MnSb compound through experimental and theoretical approaches. Temperature-dependent magnetization data in-

dicates an anomalous decrease in magnetization below ∼120 K, which is expected due to the SRT [8]. Magneto-transport data indicates that negative magneto-resistance first increases from room temperature to the SRT temperature (T_{SR}) ∼120 K, but then decreases and becomes positive in very low-temperature region. The AHC shows temperature independent behavior from room temperature to T_{SR}, followed by a drop and sign reversal at low temperatures. A detailed scaling analysis of anomalous Hall data indicates that the intrinsic Berry curvature is predominantly responsible for the AHE above T_{SR} and the obtained value of the intrinsic AHC is about 310 S/cm. Whereas, below T_{SR} the AHE is mainly governed by the extrinsic skew scattering mechanism over the intrinsic Berry curvature and the obtained value of the intrinsic AHC is about -28 S/cm. First-principles calculations reveal that changes in the sign and magnitude of intrinsic AHC is originated from the modification in Berry curvature linked with the band splitting near the Fermi level. The modification in Berry curvature arises due to the reconstruction of the electronic band structure under the variation of spin orientation from the c-axis to the ab plane within the crystal system around the SRT. Besides the AHE, we report the THE, which is independent of temperature in low temperature region below T_{SR}, while indicating a large dependence on temperature above T_{SR}. A detailed micromagnetic simulation confirms that the emergence of skyrmionic bubbles due to competition of the uniaxial MCA with different energies is responsible for the THE below T_{SR}, which is also supported by the magnitude (in nΩ.cm) and temperature independent behavior of THE. In contrast, above T_{SR} the simulation findings suggest that the comparatively large ($\mu\Omega$.cm) and temperature-dependent behavior of the THE could be attributed to the microscopic non-coplanar spin texture, rather than being solely driven by skyrmionic bubbles.

6.2 Methods

The polycrystalline MnSb binary compound is prepared by the standard arc-melting method [20, 21]. The constituent elements (purity higher than 99.9%) of the intermetallic system are melted in a water-cooled copper hearth under argon atmosphere (purity better than 99.999%). The sample is remelted five times to ensure homogeneous mixing of the constituents. A negligible weight loss of 1% was noticed after the melting of the sample. The obtained ingot was then vacuum sealed in a quartz tube, followed by annealing at 1073 K for three days to achieve good homogeneity. The chemi-

cal composition is verified using the energy dispersive analysis of x-ray technique. The average composition is found to be $Mn_{0.99}Sb_{1.00}$, which corresponds to MnSb. A small piece of the sample is powdered, and room temperature x-ray diffraction (XRD) is performed in the Rigaku X-ray diffractometer (wavelength ∼1.54 Å) for structural analysis. The direct current (DC) magnetization measurements are performed using a physical property measurement system (PPMS) of quantum design(QD). The polished rectangular piece of the dimension $4 \times 2 \times 0.7$ mm^3 was used for temperature and magnetic field-dependent transport measurements using a cryogen-free measurement system (Cryogenic, CFMS). The transport measurements are performed by the four-probe method. To remove the longitudinal resistivity contribution in the Hall data due to voltage probe misalignment, we have anti-symmetrized the Hall resistivity data by using the formula $\rho_{xy} = [\rho_{xy}(+H) - \rho_{xy}(-H)]/2$. On the other hand, we have symmetrized the magneto-resistance data by using the formula $\rho_{xy} = [\rho_{xy}(+H) + \rho_{xy}(-H)]/2$ to remove the transverse resistivity contribution in the magneto-resistance.

The electronic band structure and magnetic properties of the MnSb compound were calculated by employing pseudopotential (PP) based density-functional theory (DFT) and plane-wave basis sets as implemented in QUANTUM ESPRESSO (QE) [22], whereas exchange-correlation potential is approximated by Perdew-Burke-Ernzerhof generalized gradient approximation (PBE-GGA) approach [23] through optimized Norm-conversing Vanderbilt PPs [24]. The kinetic energy cutoff of 80 Ry is used for the calculation. The Gaussian smearing value (0.01 Ry) is used both for the self-consistent (SC) and non-self-consistent (NSC) calculations to carry out electronic integration over the Brillouin zone (BZ). We have used the WANNIER90 tool (implemented within QE) in order to compute the Wannier interpolated bands, Berry curvature, and AHC [22, 25, 26, 27]. The Monkhorst-Pack **k**-grid of $8 \times 8 \times 8$ of the BZ is considered for calculations, viz.: SC, NSC, and WANNIER90. We found that the Mn d-orbitals and Sb p-orbitals used as the projection for the WANNIER90 calculations provide good interpolation. A denser BZ **k**-grid of $100 \times 100 \times 100$ is taken to calculate the intrinsic AHC. Through the adaptive refinement technique, a further fine mesh of $5 \times 5 \times 5$ is added around the points wherever the mode of the Berry curvature ($|\Omega(\mathbf{k})|$) exceeds 100 bohr^2. The calculations are carried out by using the refined lattice parameters obtained from the experiment.

6.3 Results and discussion

6.3.1 Structural characterization

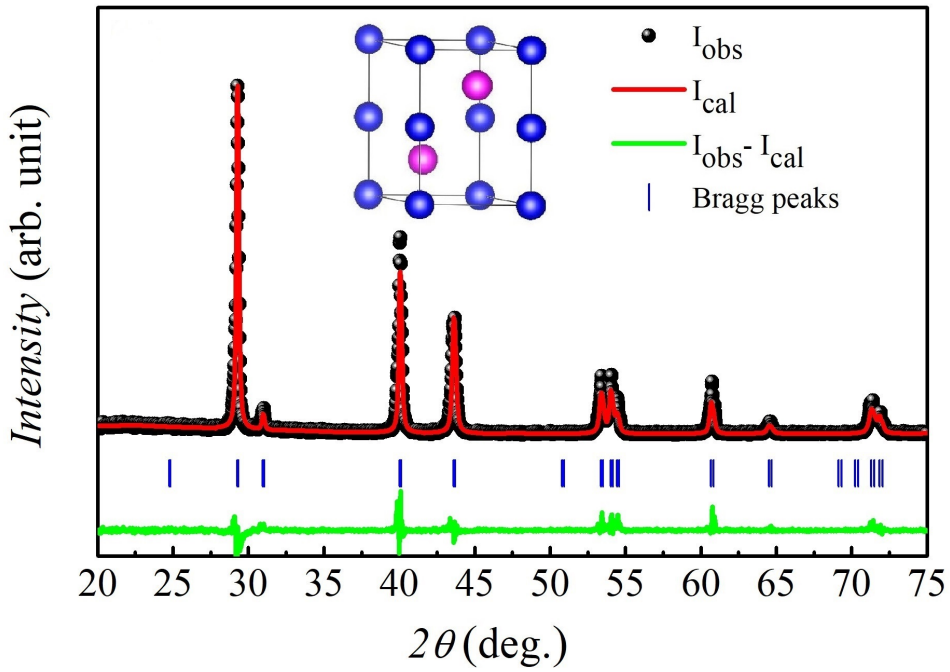

Figure 6.1: Rietveld profile fitting of the room temperature x-ray diffraction pattern of the MnSb compound. The observed (I_{obs}), calculated (I_{cal}), and the difference between observed and calculated profiles (I_{obs}-I_{cal}) are shown by black sphere, red continuous line, and green continuous line, respectively. The blue tick bars indicate the Bragg peak positions. Inset displays crystal structure of MnSb. The blue and magenta spheres indicate the Mn and Sb atoms, respectively.

The XRD pattern at room temperature was collected to investigate the crystal structure of the MnSb binary compound. We performed Rietveld refinement of the XRD data by assuming the reported hexagonal space group $P6_3/mmc$ [Fig. 6.1] [28, 29], using the FULLPROF software package [30]. In the refinement, the Mn and Sb atoms were considered at 2a (0, 0, 0) and 2c (0.67, 0.33, 0.75) Wyckoff positions, respectively. It can be noticed from Fig. 6.1 that the observed and calculated peak profiles are well matching with each other, which suggests that the MnSb compound crystallizes in a single phase, as there is no evidence of the impurity peaks in the XRD pattern. The refined lattice parameters a and c are found to be ∼4.14 Å and ∼5.76 Å, which is in good agreement with the literature [28]. The inset of Fig. 6.1 shows the crystal structure of MnSb, built in VESTA software [31] using refined parameters.

6.3.2 Magnetization and resistivity measurements

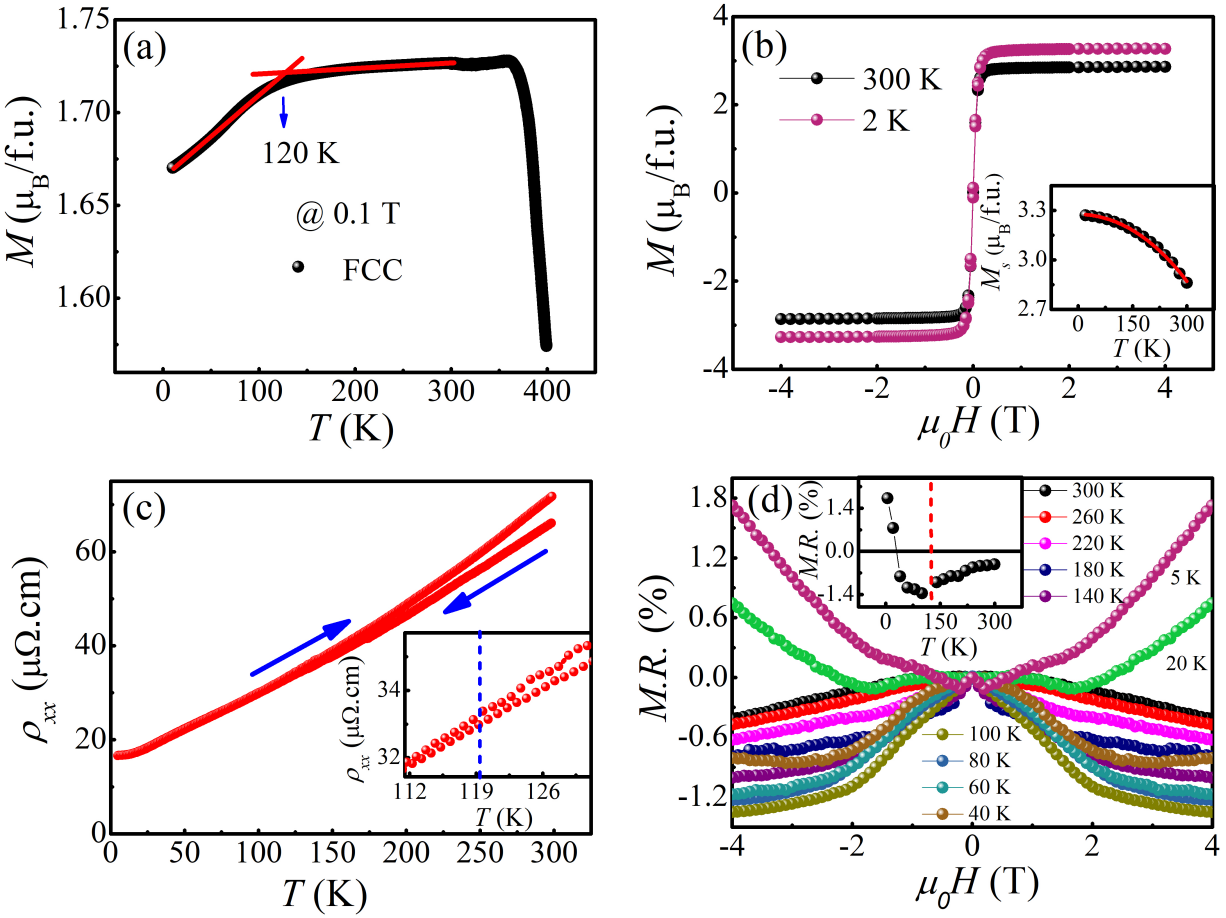

Figure 6.2: (a) Temperature-dependent magnetization curve at 0.1 T magnetic field. (b) The isothermal field-dependent magnetization at 2 K and 300 K temperatures. Inset shows the fitting of saturation magnetization (M_s) vs temperature (T) with empirical relation $M_s=M_0[1-(T/Tc)^2]^{1/2}$. The black dots and the red continuous line in the inset represent the M_s vs T data and the fitted curve, respectively. (c) Resistivity (ρ_{xx}) versus temperature (T) plot in cooling and heating sequence. The inset shows zoomed view of the ρ_{xx} versus T data around spin reorientation transition. (d) The plot of magneto-resistance (M.R.) at different temperatures. Inset shows the variation of M.R. at 4 T as a function of temperature.

The temperature variation of magnetization [$M(T)$] is measured in a temperature range of 2-400 K under the magnetic field of 0.1 T, shown in Fig. 6.2(a). The $M(T)$ curve shows an anomalous decrease in magnetization below temperature around 120 K. A magnetic transition close to 120 K has been previously observed in a similar composition, and this transition has been established as the spin reorientation transition (SRT) through neutron diffraction study [8]. The reported neutron diffraction study indicates that the spin associated with Mn atoms changes its orientation from the magnetic easy axis parallel to the c-axis to the ab-plane at low temperatures. In high temperature region above

room temperature, the M-T data exhibits a sharp decrease in magnetization above 356 K that might be related to the onset of ferromagnetic to paramagnetic phase transition, which is expected around 600 K [5, 32].

Fig. 6.2(b) presents the field-dependent magnetic isotherms (*M(H)* curves) at 2 K and 300 K. The negligible hysteresis is due to the soft magnetic nature of the MnSb compound. The *M(H)* curves show similar behavior in the entire temperature range of 2-300 K. To calculate the Curie temperature (T_c) of the present compound, the saturation magnetization (M_s) versus temperature ($M_s(T)$) data obtained from the *M(H)* curves [black spheres in the inset of Fig. 6.2(b)] were fitted by the empirical law $M_s = M_0[1-(T/Tc)^2]^{1/2}$ [red curve in the inset of Fig. 6.2(b)] [33]. From this fitting, the T_c was found to be ∼600 K, which is in good agreement with the value reported in the literature [32]. The saturation magnetization of the present compound is found to be ∼3.3 μB/f.u. at 2 K, which agrees well the value reported in literature [32, 34, 35].

Fig. 6.2(c) shows the monotonous increase in the longitudinal resistivity with temperature, which illustrates the metallic behavior of the present compound. We have collected the resistivity data in both cooling and heating mode of temperature variation, which exhibits a thermal hysteresis above T_{SR} ∼120 K. The thermal hysteresis in pre-SRT region confirms the thermally driven and first order nature of spin reorientation phase transition [36, 37].

Fig. 6.2(d) displays the magneto-resistance (M.R.) at different temperatures calculated by performing the field dependent resistivity measurement. The M.R. is calculated by using the following relation [10]-

$$M.R. = \frac{\rho_{xx}(H) - \rho_{xx}(0)}{\rho_{xx}(0)} \tag{6.1}$$

where ρ_{xx}(H) and ρ_{xx}(0) are longitudinal resistivities at a particular field and at zero field, respectively. The maximum value of M.R. is ∼1.7% at temperature 20 K. The inset of Fig. 6.2(d) indicates that the negative M.R. at 4 T increases with the lowering of the temperature, but below T_{SR}, it started to decrease and becomes positive in very low-temperature region, which might be originated from the spin orientation form the magnetic easy axis parallel to the c-axis to the ab-plane below T_{SR},

as a similar unusual behavior of M.R. is anticipated around the SRT [12, 38, 39, 40]. In the high temperature region above T_{SR}, the orientation of spin associated with the Mn atom is restricted along the easy axis i.e., c-axis and upon the application of magnetic field the fluctuations of magnetic moments decrease, which may give rise to negative M.R [12, 38]. Whereas, in low temperature region below T_{SR} the negative M.R. decreases and becomes positive at very low temperatures, which might be related to the orientation of Mn spin in the ab-plane or out of the direction of easy axis. The spin oriented out of the direction of the easy axis may experience increase in fluctuations on the the application of magnetic field and gives rise to positive M.R. [12, 38, 41]. The literature suggests exotic effects of the spin reorientation on the Hall effect such as manipulation of the sign and magnitude of the AHE as a function of temperature [11, 12, 13, 14]. Therefore, further we investigated the Hall effect in the MnSb compound.

6.3.3 Anomalous Hall measurement

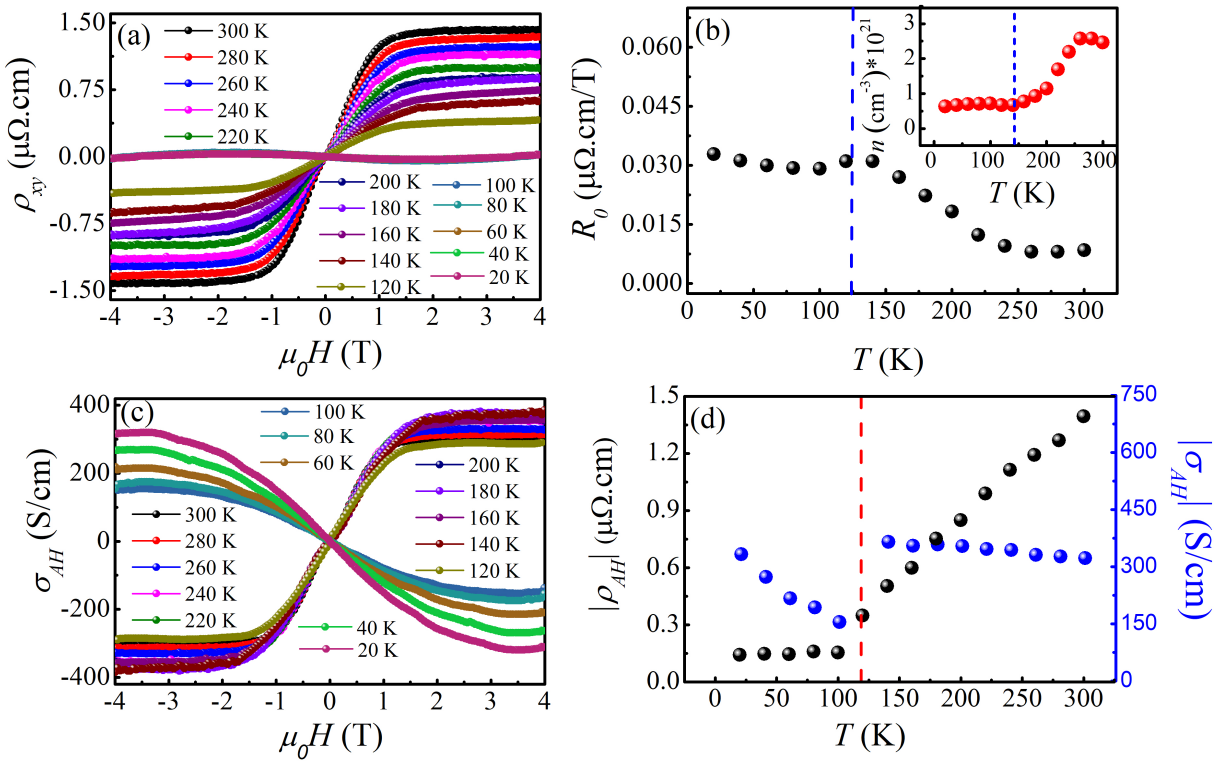

Figure 6.3: (a) Hall resistivity curves at different temperatures. (b) Variation of ordinary Hall coefficient with temperature. Inset shows carrier concentration versus temperature plot. (c) Anomalous Hall conductivity (AHC) curves at different temperatures. (d) Variation of the AHC and the anomalous Hall resistivity with respect to temperature.

Hall measurements are performed in the temperature range of 20-300 K to investigate the anomalous transport behavior of the MnSb compound. The Hall resistivity ρ_{xy} were recorded at different temperatures up to a magnetic field of $\pm$4 T [Fig. 6.3(a)], which is associated with a sign change below T_{SR}, may be related to the SRT. In a general sense, the total Hall resistivity (ρ_{xy}) consists of two parts, namely ordinary Hall and anomalous Hall, and can be written as [42, 43]-

$$\rho_{xy} = R_0 H + R_s M_s \tag{6.2}$$

where R_0 and R_s are the ordinary and anomalous Hall coefficients, respectively. M_s corresponds to the saturation magnetization and $R_s M_s$ represents the magnitude of anomalous Hall resistivity (ρ_{AH}). The ρ_{xy} increases steeply up to $\sim$ 1 T field, which is observed due to the presence of AHE. At the higher field region (>1 T), ρ_{xy} changes linearly and shows a positive slope with the magnetic field, which is due to the ordinary Hall effect [44].

To separate out the ordinary and anomalous Hall contributions, we performed fitting of the ρ_{xy} versus H data by using the Eq. (2) in the higher field region (>1 T). The fitting of the ρ_{xy} versus H at different temperatures provides the value of R_0 and $R_s M_s$ that corresponds to the slope and intercept of the fitted line. Fig. 6.3(b) shows a temperature variation of R_0 obtained from the fitting. The positive value of R_0 in the whole temperature range (20-300 K) reveals that holes are the dominating charge carriers in transport. The carrier concentration (n) as depicted in the inset of Fig. 6.3(b), determined by the expression $n = \frac{1}{eR_0}$, was found to be $\sim 0.7\times10^{21}$cm^{-3} and $\sim 3\times10^{21}$cm^{-3} at 20 K and 300 K, respectively. There is a monotonous change in the value of R_0 and n around T_{SR}, which may be related to the SRT. The AHC has been calculated by using the relation [45, 46]-

$$\sigma_{AH} = \frac{\rho_{AH}}{{\rho_{AH}}^2 + {\rho_{xx}}^2} \tag{6.3}$$

The field-dependent ρ_{AH} at different temperatures are calculated by subtracting the ordinary Hall contribution from the field-dependent ρ_{xy}. The calculated field-dependent AHC by using Eq. (3) at different temperatures is shown in Fig. 6.3(c), which clearly demonstrates the sign change below T_{SR}. The value of AHC at 20 K and 300 K is 322 S/cm and 332 S/cm, respectively. Fig. 6.3(d)

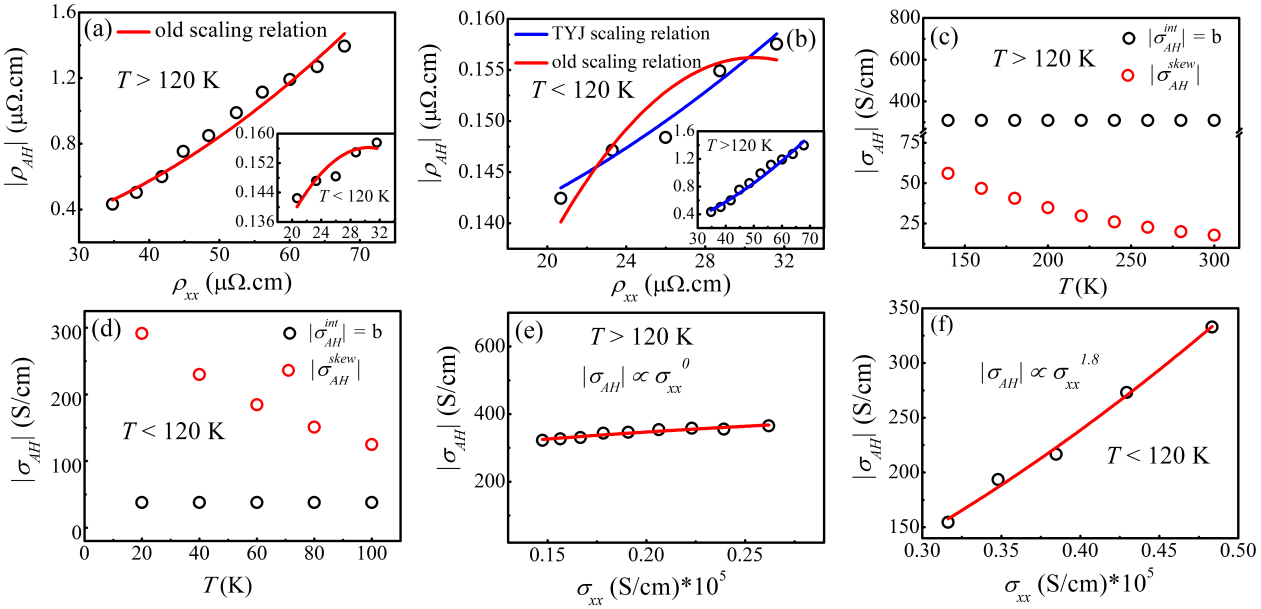

Figure 6.4: (a) Fitting of anomalous Hall resistivity ($|\rho_{AH}|$) vs longitudinal resistivity (ρ_{xx}) data above the spin reorientation transition temperature (T_{SR}) using the conventional scaling relation. Inset shows the same fitting below T_{SR}. The black hollow spheres and the red continuous line represent the experimental data and the fitted curve obtained by the conventional scaling, respectively. (b) Comparison between the fitting of $|\rho_{AH}|$ vs ρ_{xx} data below T_{SR} using the conventional scaling and the TYJ scaling relations. Inset shows the fitting of $|\rho_{AH}|$ vs ρ_{xx} data above T_{SR} using the conventional scaling relation. The black hollow spheres, and the red and blue continuous lines represent the experimental data and the fitted curves obtained by the conventional scaling and the TYJ scaling, respectively. (c) and (d) Different contributions in anomalous Hall conductivity (σ_{AH}) above and below T_{SR}, respectively. (e) and (f) Variation of σ_{AH} with longitudinal conductivity (σ_{xx}) above and below T_{SR}, respectively. The black hollow spheres and the red continuous line represent the experimental data and the fitting using the relation $\sigma_{AH} \propto \sigma_{xx}^{\alpha}$.

shows that the AHC is nearly independent of the temperature above T_{SR}, while below T_{SR}, it shows temperature-dependent behavior as compared to the ρ_{AH}. This observation suggests that above T_{SR}, the intrinsic Berry curvature is primarily attributed to the AHE, while the extrinsic skew scattering is the dominating mechanism below T_{SR}.

To quantitatively reveal the contributions of the intrinsic and extrinsic mechanisms to the AHE, the $|\rho_{AH}|$ versus ρ_{xx} data [black hollow spheres in Fig. 6.4(a) and inset of Fig. 6.4(a)] is fitted [red continuous line in Fig. 6.4(a) and inset of Fig. 6.4(a)] by using the conventional scaling relation [44, 47, 48, 49, 50, 51]-

$$|\rho_{AH}| = a.\rho_{xx} + b.{\rho_{xx}}^2 \tag{6.4}$$

where parameters *a* and *b* contain information about extrinsic skew scattering and the combined effect of extrinsic side jump and intrinsic contribution, respectively. The fitting by using the above scaling relation in high temperature region above T_{SR} [Fig. 6.4(a)] indicates good fitting, while in low temperature region below T_{SR} the scaling relation shows appreciable deviations from the trend of experimental data, which indicates the breakdown of the conventional scaling relation below T_{SR}. A similar breakdown of the conventional scaling relation in the low temperature region has been observed in the $Mn_{1.5}Ga$ film, where the ρ_{AH} does not show significant change as a function of the ρ_{xx} [52]. This deviation of the conventional scaling relation from the experimental data has found its root in negligible temperature-dependent component in the skew scattering mechanism as compared to the impurity component [52].

Tian *et al.* argued that the conventional scaling relation shows significant deviation from the experimental data for those systems, where the temperature-dependent component (phonons) have a negligible effect to the skew scattering mechanism in the AHE compared to the impurity. For such systems, they have derived a new scaling relation ($|\rho_{AH}| = a'.\rho_{xx0} + b.{\rho_{xx}}^2$) from the conventional scaling relation, after considering the phonon and impurity as an independent source of skew scattering mechanism ($a.\rho_{xx} = a'.\rho_{xx0} + a''.\rho_{xxT}$, where ρ_{xx0} and ρ_{xxT} is residual resistivity and phonon induced resistivity, respectively) and taking the coefficient $a'' \approx 0$ for the negligible phonon contribution in the skew scattering [53]. Nowadays, this new scaling relation is widely termed as the TYJ

scaling relation [47, 54, 55, 56].

Therefore, we have used the TYJ scaling relation in the low temperature region of the MnSb compound, where ρ_{AH} does not exhibit significant variation with the ρ_{xx}. Remarkably, we found a good fit [blue continuous line in Fig. 6.4(b)], which is clearly reflected by the comparison of the fitted curves obtained by both the scaling relations [Fig. 6.4(b)]. The TYJ scaling model perfectly follows the experimental data not only below T_{SR}, but also above T_{SR}, as shown in the inset of Fig. 6.4(b). This finding suggests that the the extrinsic contribution to skew scattering from temperature-dependent component is negligible in the case of the MnSb compound and the AHE is originated by impurity-induced skew scattering, and the combined side jump and intrinsic mechanisms. The value of $a'.\rho_{xx0}$ and the coefficient b in the high-temperature region is obtained to be $\sim 8.86 \times 10^{-8}$ Ω.cm and $\sim$ 310 S/cm, respectively, whereas in the low-temperature region, $a'.\rho_{xx0} \sim 1.25 \times 10^{-7}$ Ω.cm and $b \sim 28$ S/cm. The value of parameter b contains the contributions in AHC due to both side jump and momentum space Berry curvature. So far, it has been experimentally infeasible to separate the contributions of side jump and intrinsic mechanism in AHC. However, the AHC due to the side jump mechanism can be estimated by using an expression $(e^2/(ha)(E_{so}/E_F)$, where E_{so} is the spin-orbit interaction energy and E_F is Fermi energy [49, 57, 58]. The physical quantities e, h, and a are the electronic charge, Planck's constant, and lattice parameter, respectively. For most of the ferromagnetic metals, E_{so}/E_F is an order of 10^{-2} [50], and hence a very small contribution of AHC is expected due to a side jump in comparison to the intrinsic part of AHC.

By using the value of $a'\rho_{xx0}$ and coefficient b, we calculated the temperature dependent magnitude of extrinsic skew scattering AHC ($|\sigma_{AH}^{skew}| = \frac{a'.\rho_{xx0}}{\rho_{xx}{}^2}$) and the magnitude of intrinsic Berry curvature AHC ($|\sigma_{AH}^{int}|$ = b) and plotted it on same scale above and below T_{SR}, as shown in Fig. 6.4(c) and Fig. 6.4(d), respectively. We can clearly see that the intrinsic contribution dominates over the skew scattering contribution in the overall AHE in the high-temperature range above T_{SR}. In comparison, the skew scattering contribution is dominating over the intrinsic contribution in low-temperature region below T_{SR}, which is consistent with the literature [5].

The dominating mechanism in the AHE can be alternatively evaluated by the exponent α using the scaling relation $|\sigma_{AH}| \propto \sigma_{xx}{}^{\alpha}$. In metallic conductors, if $\alpha = 0$, the intrinsic mechanism contributes

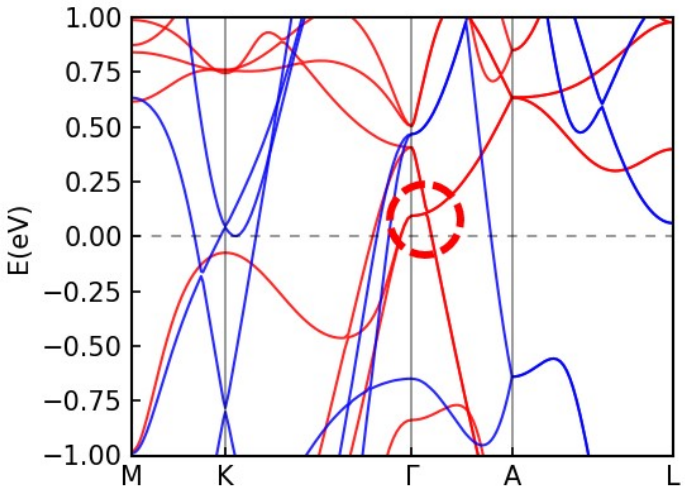

Figure 6.5: Spin-polarized electronic band structure of MnSb compound. The red and blue lines represent the majority and minority spin states. The red circles represents the region of our interest around high symmetry point Γ

largely to the AHE [47, 58, 59, 60], and if α is 2, the skew scattering mechanism dominates in AHE [47, 47, 54, 60, 61]. The exponent α determined by fitting is turned out to be $\sim$0.2, close to 0 above T_{SR} [Fig. 6.4(e)], whereas below T_{SR}, the α is 1.8, close to 2 [Fig. 6.4(f)], which further supports the observation that in high-temperature region, the AHE is primarily governed by the intrinsic Berry curvature, while in the low-temperature region it is mainly originated by extrinsic skew scattering mechanism. Above T_{SR}, the obtained value of intrinsic AHC along with the sign is about 310 S/cm, whereas below T_{SR} the value is about -28 S/cm. To explore the possible reason behind the change in sign and magnitude of intrinsic AHC, we performed the first principles calculations for the different spin configurations expected around T_{SR}.

6.3.4 First-principles calculations

The theoretical calculations of the MnSb compound have been carried out by using lattice parameters obtained from the Rietveld refinement of XRD data. Our calculated magnetic moment for the stoichiometric MnSb is found about 3.43 μ_B/f.u., which is in good agreement with the experimental value. The spin-polarized band structure of the MnSb compound is shown in Fig. 6.5. The red and blue color represent the band structure resulting from majority and minority spin states, respectively. An interesting linear touching point between the valence and conduction band is observed along Γ-A

direction comprising from the majority spin states, as shown inside the red circle in Fig. 6.5.

Figs. 6.6(a) and (d) show the crystal structure with the inclusion of magnetic spin of Mn atom along the c-axis and within the ab-plane. These structures are built in VESTA software [31] using refined parameters and considering the magnetic spins. Since spin-orbit coupling (SOC) plays an important role in determining the AHC for ferromagnetic materials, we calculated the band structure of MnSb with the SOC and by setting the magnetization along the c-axis, as depicted in Fig.6.6(b). In the electronic band structure for this magnetic configuration along the c-axis, a red circular region highlights band splitting, accompanied by linear band crossings near the Fermi level in proximity to the high symmetry Γpoint. This band splitting produces the substantial Berry curvature [Fig.6.6(c)] in the Brillouin zone, which may lead to the large intrinsic anomalous Hall conductivity (AHC). To calculate the Berry curvature and intrinsic AHC, the tight binding Hamiltonian is constructed using maximally localized Wannier functions [25, 27]. The intrinsic AHC was calculated using kubo formula [62]

$$\sigma_{\alpha\beta} = -\frac{e^2}{\hbar}\sum_{n}\int \frac{d^3k}{(2\pi)^3}\Omega^{n}_{\alpha\beta} f_n \tag{6.5}$$

where Berry curvature Ω can be written as sum over eigen state using Kubo formula [**?**]

$$\Omega^{n}_{\alpha\beta} = i\sum_{n\neq n'} \frac{\langle n|\frac{\partial H}{\partial k^{\alpha}}|n'\rangle\langle n'|\frac{\partial H}{\partial k^{\beta}}|n\rangle - (\alpha \leftrightarrow \beta)}{(\epsilon_n - \epsilon'_n)^2} \tag{6.6}$$

where $|n\rangle$ and ϵ_n are the energy eigenstate and eigenvalue of Hamiltonian H, respectively. f_n is the Fermi distribution function.

From the integration of Berry curvature in the Brillouin zone, we found the large intrinsic AHC about ∼625 S/cm [Fig. 6.7]. Notably, this value is larger as compared to the other binary compounds [40, 63, 64]. This large value of the theoretical intrinsic AHC is of the order of experimental value ∼ 310 S/cm. As this compound undergoes the spin-reorientation transition around 120 K, characterized by the rotation of spins from the c-axis to the ab-plane [Fig. 6.6(d)], we incorporated this phenomenon in the theoretical calculation. Specifically, we calculated the band structure of MnSb in the presence of SOC by setting the magnetization direction within the ab-plane, as shown in Fig.6.6(e). Fig. 6.6(e) reveals a significant change in the electronic band structure in this magnetic

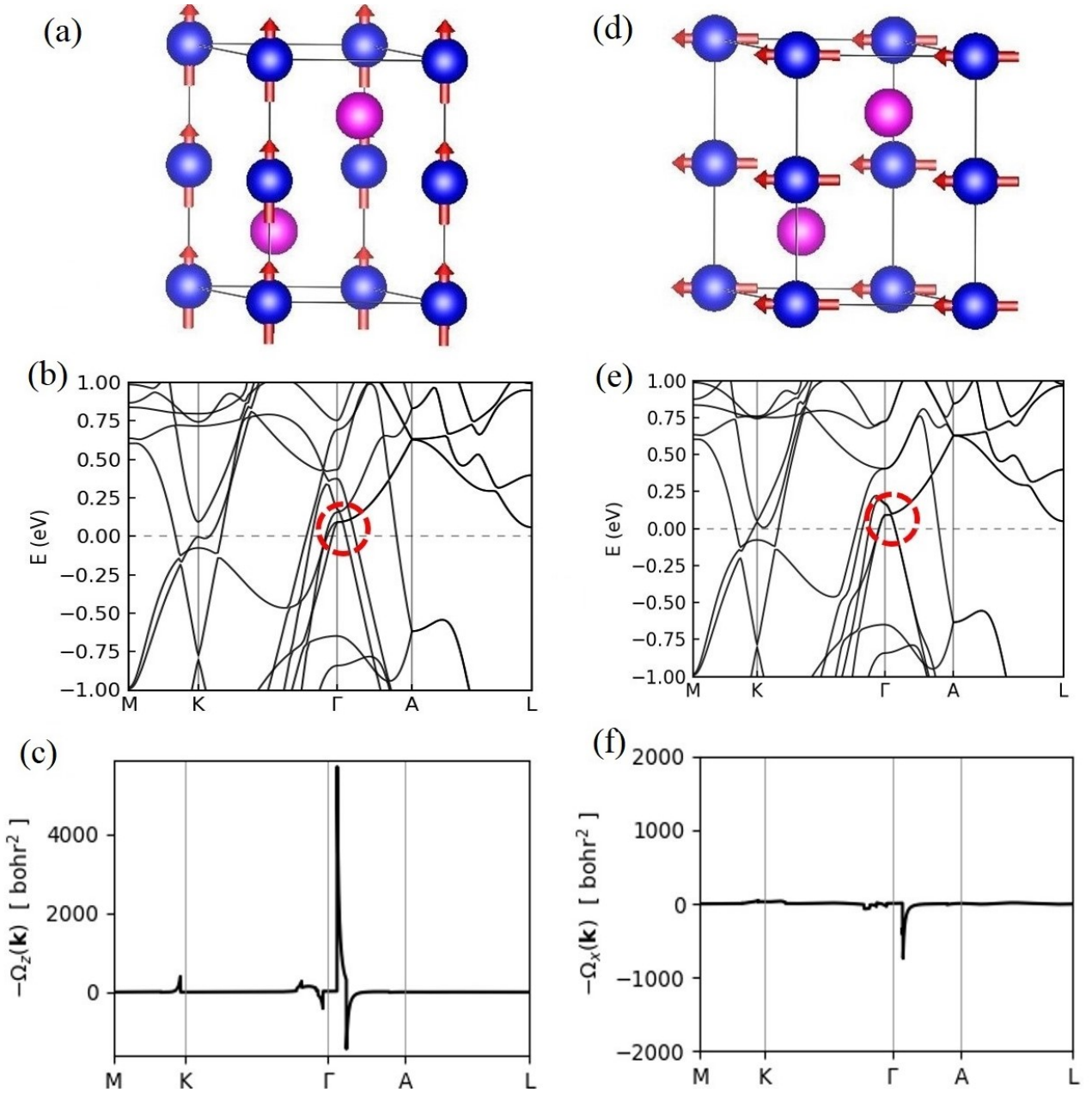

Figure 6.6: (a) Crystal structure with the magnetic spins aligned along the c-axis. (b) The electronic band structure of MnSb considering the magnetic spin aligned along the c-axis. The red circle represents the region of our interest around high symmetry point Γ. (c) Distribution of the Berry curvature along high symmetry path in the Brillouin zone for the magnetic spin aligned along the c-axis. (d) Crystal structure with the magnetic spins within the ab-plane. (e) The electronic band structure of MnSb considering the magnetic spin within the ab-plane. The red circle represents the region of our interest around high symmetry point Γ. (f) Distribution of the Berry curvature along high symmetry path in the Brillouin zone for the magnetic spin within the ab-plane.

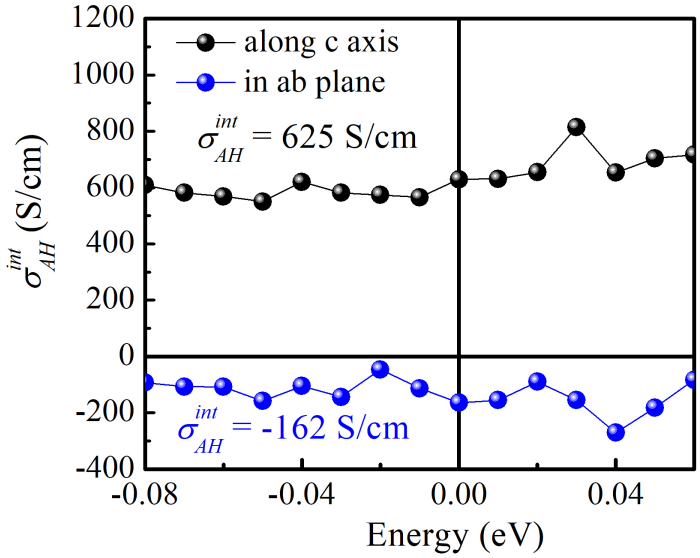

Figure 6.7: Variation of intrinsic anomalous Hall conductivity as a function of energy. The Fermi energy is set to 0 eV.

configuration.

Notably, the pre-existing band splitting is less and the linear touching points near the high symmetry Γpoint vanish. The dominated Berry curvature has opposite sign near the Γpoint [Fig. 6.6(f)] in contrast to the Berry curvature assuming the magnetic spin in c-direction. Interestingly, we found the intrinsic AHC about -162 S/cm [Fig. 6.7], which is nearly 4 times lower than the intrinsic AHC calculated considering the magnetic moment in the c-direction. The decrease in AHC is attributed to the negligible band splitting as well as the vanishing of linear band crossings, which were present in the band structure when considering the moment in the c-direction [Fig. 6.6(b)]. Notably, in the magnetic configuration within the ab-plane, the intrinsic AHC becomes negative, aligning with experimental findings. This change in AHC polarity may find its roots in the reversal of the sign of Berry curvature, a consequence of the electronic band structure reconstruction during the spin reorientation transition. It is worth highlighting that our experimental findings align with several aspects of our theoretical calculations. For example, we observe a decrease in the AHC below T_{SR}, and a favorable change in the intrinsic AHC sign, consistent with our theoretical predictions. However, it is important to acknowledge that there are difference in the magnitude of AHC between the experimental and theoretical results. These differences might be possible due to the inherent assumptions made in our theoretical modeling and the specific experimental conditions during material synthesis.

6.3.5 Topological Hall analysis

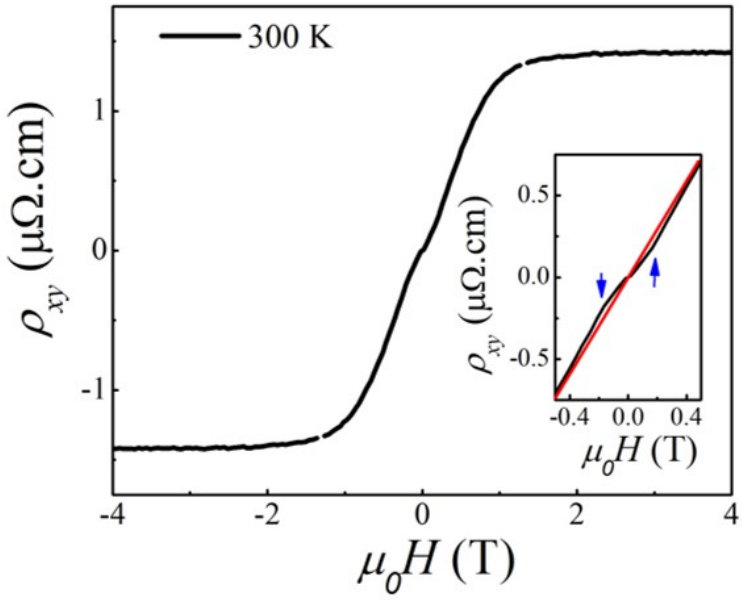

Figure 6.8: Hall data at 300 K. Inset shows the zoomed view of the Hall data in low magnetic field region.

Fig. 6.8 demonstrates that the Hall data has a dip type anomaly, which is typically a signature of the presence of THE and the non-coplanar magnetic texture with non-zero spin chirality [9]. Inset of Fig. 6.8 represents the clear view of the dip type anomaly in low magnetic field region. In high magnetic field region, the total Hall resistivity can be expressed as Eq. (6.2) as topological Hall resistivity vanishes in fully spin polarized state. To calculate topological Hall resistivity from the Hall data in low magnetic field region, we have first calculated the coefficients R_0 and Rs in Eq. (6.2) by using high field (>2 T) Hall data and *M(H)* data. For that, we have plotted the ρ_{xy}/H versus M/H data and performed linear fitting with the reduced relation [Eq. (6.2) divided by field H]-

$$\frac{\rho_{xy}}{H} = R_0 + R_s \frac{M}{H} \tag{6.7}$$

By using the obtained value of coefficients, we calculated Hall resistivity in the whole magnetic field region (0-4 T). To extract the topological Hall resistivity, we subtracted the calculated Hall resistivity from the experimental Hall resistivity. The combined plot of experimental Hall (black sphere), calculated Hall (by using M-H and magnetoresistance data) (red line) and topological Hall resistivity (blue line) at different temperatures is shown in Fig. 6.9 (a-d). Fig. 6.9 (d) indicates the

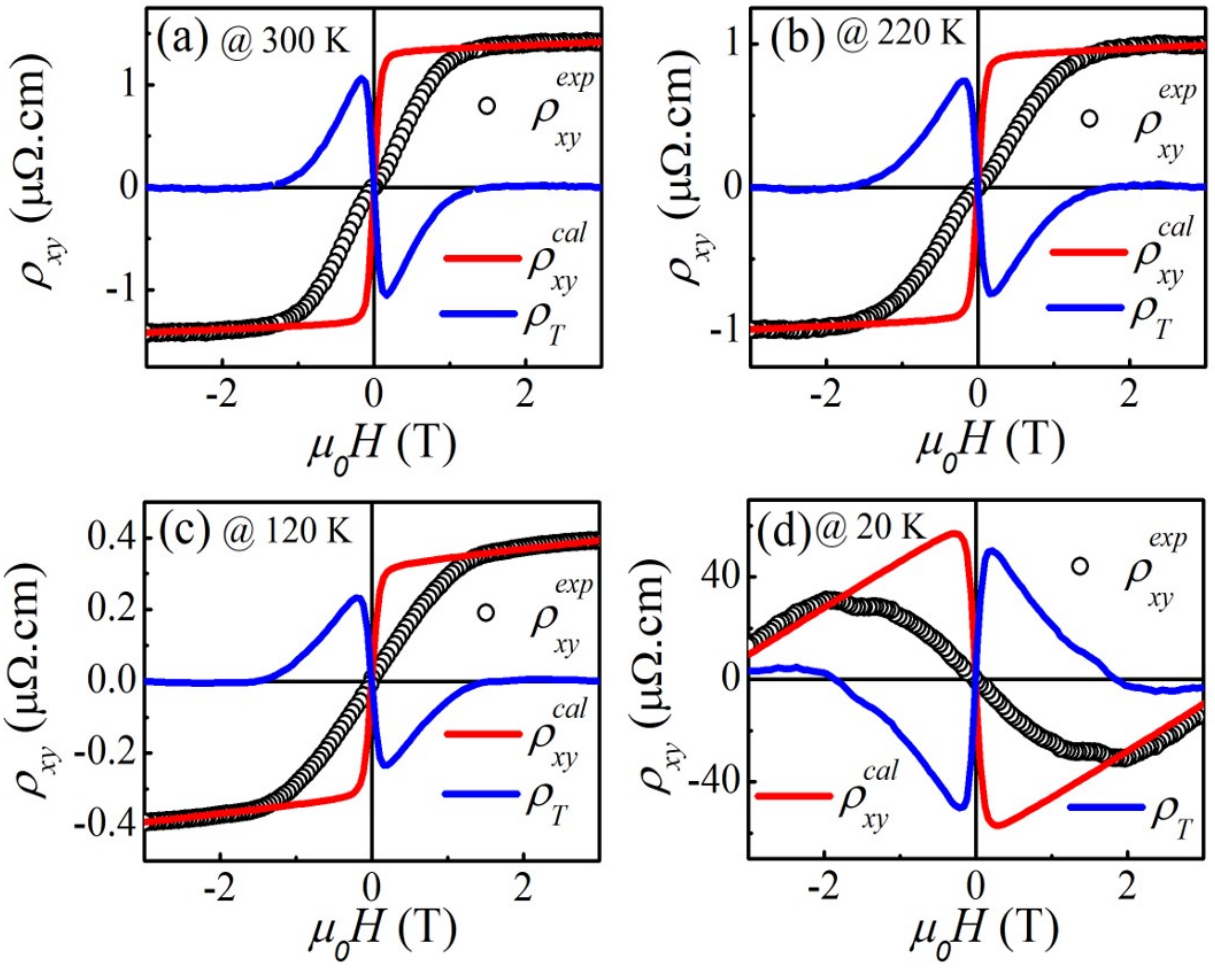

Figure 6.9: (a-d) Combined plot of experimental (black sphere), calculated (red line), and topological Hall (blue line) resistivity at 300 K, 220 K, 120 K, and 20 K, respectively.

sign reversal of THE at 20 K, which might be related to the SRT.

The topological Hall resistivity at different temperatures is shown in Fig. 6.10 (a), which indicates the THE is maximum around the magnetic field of 0.15 T. The topological Hall resistivity as a function of temperature is shown in Fig. 6.10 (b), which demonstrates that the topological Hall resistivity is independent of temperature below T_{SR}, whereas largely dependent on temperature above T_{SR}. To clearly observe the variation in the topological Hall resistivity with the magnetic field (H) and temperature (T), we create a contour plot [Fig. 6.11] of the H-T phase diagram. The contour plot clearly indicates that THE is maximum around the region of 0.15 T and is independent at temperatures below T_{SR}, while above T_{SR}, it increases to a great extent with increase in temperature. Notably, the magnitude of topological Hall resistivity is the low-temperature region below T_{SR} is in the order of nΩ.cm, whereas in the high-temperature region above T_{SR}, the topological Hall resistivity is in

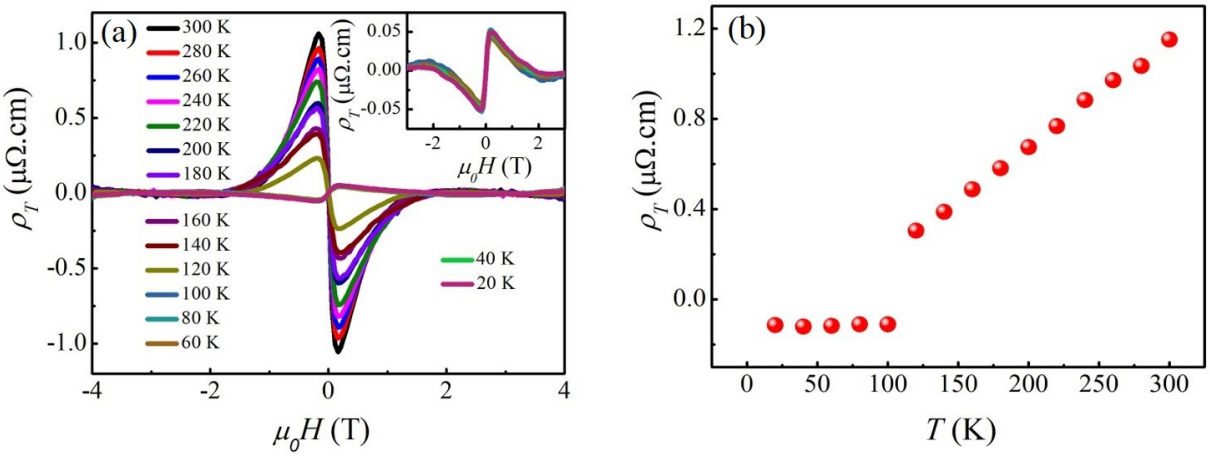

Figure 6.10: (a) Topological Hall resistivity at different temperatures. (b) Variation of the topological Hall resistivity as a function of temperature.

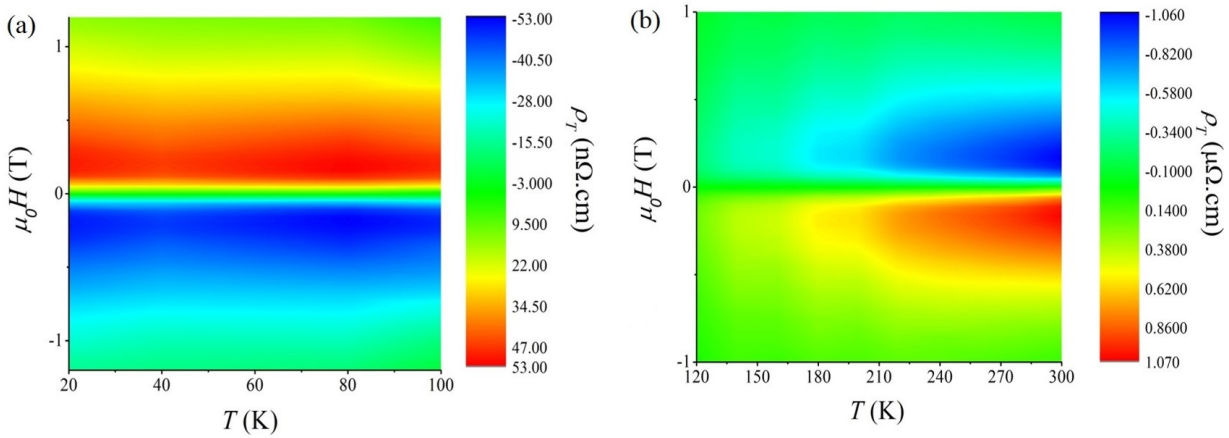

Figure 6.11: (a) Contour plot of topological Hall resistivity as a function of temperature and magnetic field below Spin reorientation transition temperature (T_{SR}). (b) Contour plot of topological Hall resistivity as a function of temperature and magnetic field above T_{SR}.

the order of $\mu\Omega$.cm. The magnitude (in nΩ.cm) and temperature independent behavior of topological Hall resistivity below T_{SR} suggest that THE is arises from the scalar spin chirality due to the topologically stable skyrmionic spin texture [9, 65, 66, 67]. Whereas, above T_{SR}, the magnitude (in $\mu\Omega$.cm) and temperature dependence of the topological Hall resistivity indicate that the THE arises not only due to the skyrmion-like spin texture, but also a major contribution is coming from some microscopic non-planar spin texture with non-zero spin chirality [9, 66, 68, 69, 70, 71].

To further confirm the formation of skyrmion like non-trivial spin texture, we have performed micromagnetic simulation. Before performing the simulation, we have calculated the energy parameters

Temperature	Saturation magnetization (A/m)	Magnetocrystalline anisotropy (K_u)	Exchange stiffness (A_{ex})
20	720015	263153.19	2.62E-11
40	716220	245179.24	2.61E-11
60	712770	193065.29	2.593E-11
80	710700	212480.62	2.585E-11
100	708630	202978.04	2.578E-11
120	705180	187545.27	2.566E-11
140	698970	180551.32	2.543E-11
160	694485	242861.23	2.527E-11
180	683100	196497.75	2.485E-11
200	675510	94411.76	2.458E-11
220	672405	222300.59	2.446E-11
240	660330	150188.20	2.403E-11
260	650187	155406.86	2.366E-11
280	634800	89943.27	2.309E-11
300	619482	85245.89	2.254E-11

Figure 6.12: (a) Table of the obtained value of saturation magnetization, uniaxial magnetocrystalline anisotropy, and exchange stiffness constant using the field dependent magnetization data at different temperatures.

like magnetocrystalline anisotropy (K) and exchange stiffness constant (A_{ex}) (linked with the exchange interaction among magnetic atoms) by using *M(H)* data (methods used to calculate these parameters are described in chapter 4). Table 6.12 shows the obtained value of M_s, K, and A_{ex} at different temperatures.

6.3.6 Micromagnetic Simulation

A detailed micromagnetic analysis was conducted using the Object Oriented MicroMagnetic Framework (OOMMF) software package [72]. Simulations is carried out on the area of 1000×1000×100 nm^3 with a 4×4×4 nm^3 cell size. The simulation energy parameters A_{ex}, *K*, and M_s (2.62×10^{-11},J/m, 2.63×10^5 J/m^3, and 7.2×10^5 A/m, respectively) were derived from the experimental *M(H)* data at 20 K. At 20 K below SRT, the simulated spin texture at zero magnetic field shows a stripe domain state by fully relaxing the randomly distributed magnetization. As increases the magnetic field, the striped domain state is gradually transformed to skyrmionic bubble texture, which is illustrated in Fig 6.13 (a-e). The most stable skyrmionic bubble type of spin texture is developed at the field of 0.155 T, as depicted in Fig 6.13 (f), aligning with experimental results that the maximum THE is

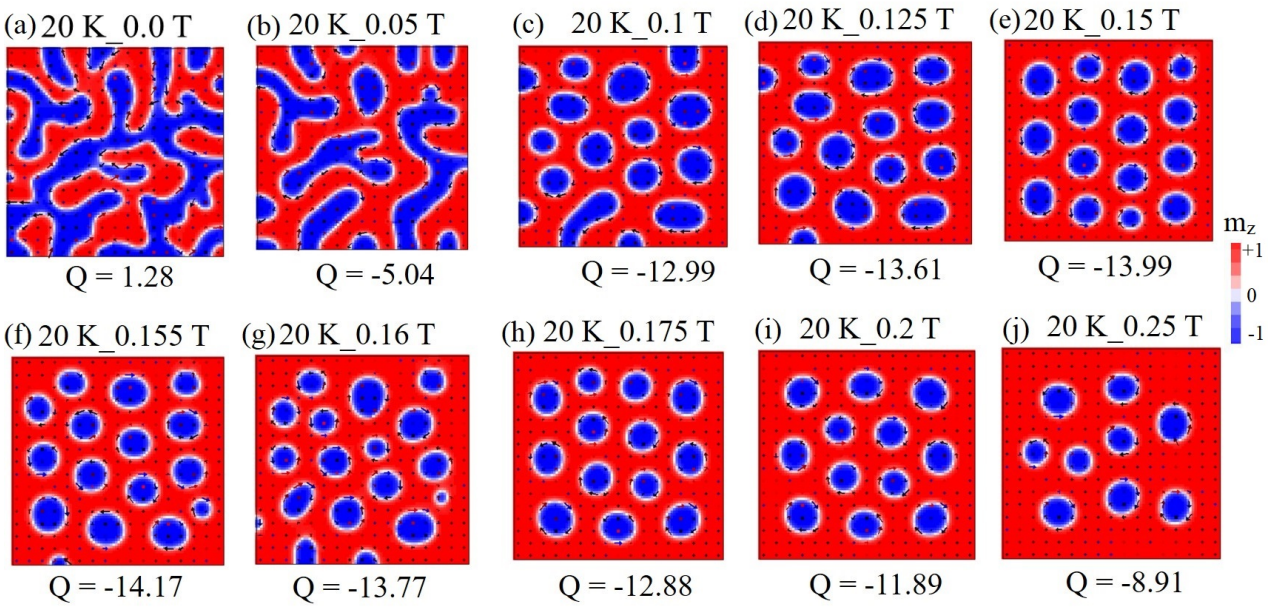

Figure 6.13: (a-j) Simulated spin textures at different magnetic field in the field range of 0-0.25 T, by using the obtained value of parameters (exchange stiffness constant= 2.62×10^{-11},J/m, uniaxial anisotropy= 2.63×10^{5} J/m^3, and saturation magnetization= 7.2×10^{5} A/m) at 20 K. First the stripe domain state was obtained by fully relaxing the randomly distributed magnetization. Then the states at different fields achieved starting from the stripe domain state as initial state. Colour bar represents the magnetic moment along z-direction. Black arrows represent the in-plane magnetization directions.

observed around the same field. As we increase the field, the skyrmionic structure is gradually distorted (the number of skyrmionic bubble decreases) and going towards spin polarized state, as shown in Fig 6.14 (g-j). As it is widely accepted that THE is directly proportional to the topological number [73, 74], and interestingly, the calculated value of the topological number in the entire simulation region initially increases with increasing magnetic field and reaches a maximum value at the field of 0.155 T, then starts decreasing with further increase in the field. This finding suggests that the theoretically simulated spin texture is aligned with experimental result and suggests that the THE in the MnSb compound may arise from the interplay of uniaxial MCA with different energies, which gives rise to the emergence of skyrmionic bubble type spin texture. The magnitude (in nΩ.cm) and temperature independent feature of THE [9, 65, 66, 67] also support the observation of skyrmionic bubble from theoretical simulation.

Above the SRT at 300 K, the simulated spin texture indicates a mixed state of striped domain and skyrmionic bubble in the entire magnetic field region and the maximum value of the topological number [Fig 6.13 (a-f)] is lower than the maximum value at 20 K. Whereas, the value of topolog-

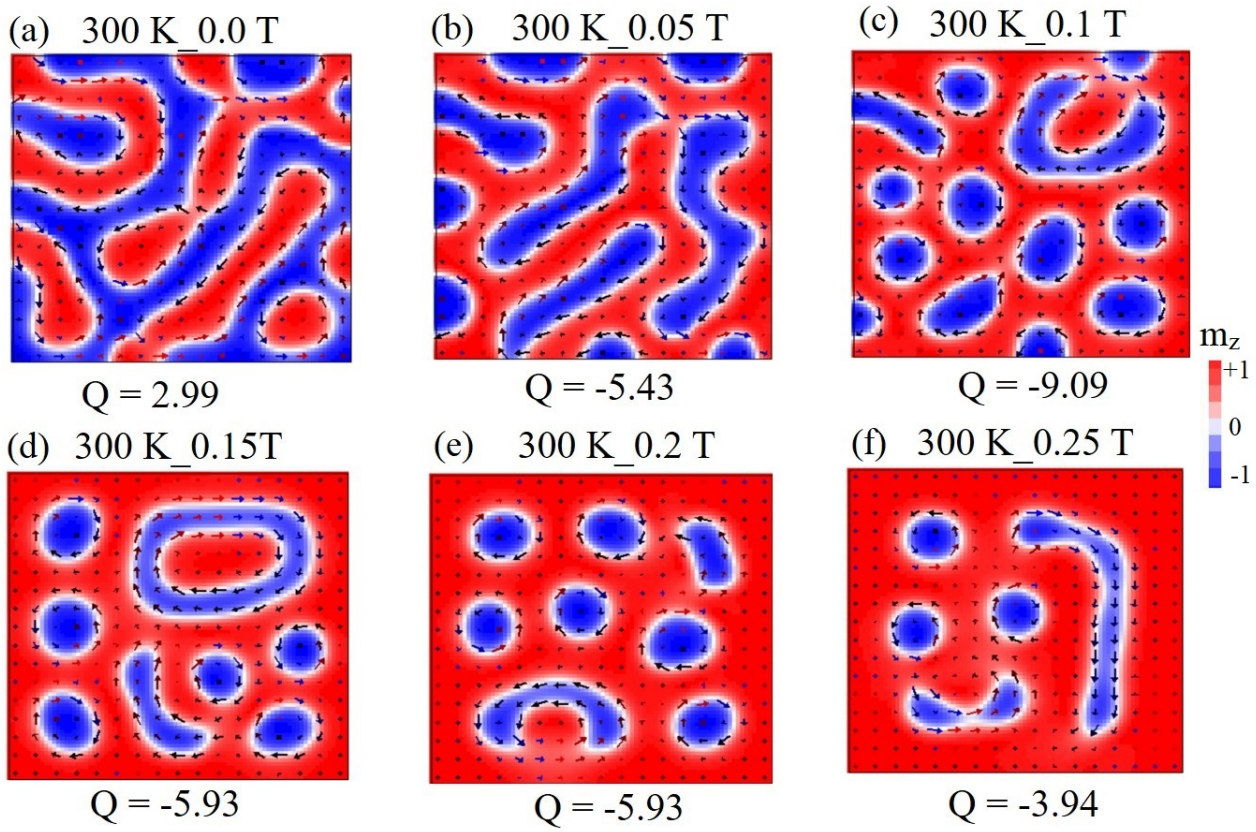

Figure 6.14: (a-f) Simulated spin textures at different magnetic field in the field range of 0-0.25 T, by using the obtained value of parameters (exchange stiffness constant= 2.25×10^{-11},J/m, uniaxial anisotropy= 8.5×10^{4} J/m^{3}, and saturation magnetization= 6.2×10^{5} A/m) at 300 K. First the stripe domain state was obtained by fully relaxing the randomly distributed magnetization. Then the states at different fields achieved starting from the stripe domain state as initial state. Colour bar represents the magnetic moment along z-direction. Black arrows represent the in-plane magnetization directions.

ical number corresponding to large THE (in $\mu\Omega$.cm) above SRT should be greater than the value corresponding to THE (in nΩ.cm) below SRT. This contradictory result as well as the temperature dependent of THE above SRT suggests that the large contribution of THE in the order of $\mu\Omega$.cm may arise due to the microscopic non-coplanar spin texture with non-zero spin chirality [9, 66, 68, 69, 70, 71, 75]. The observed sign reversal in the THE might be related to the opposite spin chirality due to rotation of magnetic moment [76] around the SRT.

6.4 Conclusion

In conclusion, the magneto-transport data show changes in the sign and magnitude of AHC below T_{SR} and around the same temperature the negative M.R. decreases and changes sign at very low temperatures. Detailed scaling analysis of the anomalous Hall data in different temperature regions reflects that the AHE above T_{SR} is mainly governed by the intrinsic Berry curvature and the calculated value of intrinsic AHC ∼310 S/cm. In contrast, below T_{SR} the AHE is mainly originated by skew scattering and the obtained value of intrinsic AHC is about -28 S/cm. The change in sign and magnitude of the intrinsic AHC in MnSb compound may be related to the anisotropic electronic band structure for different spin orientations around T_{SR}. In addition, the further analysis of the Hall data and theoretically simulated spin texture reveal the presence of THE as a result of the emergence of skyrmionic bubbles, while the larger contribution to THE above T_{SR} probably arises from the microscopic non-coplanar spin textures.

References

[1] X. Chong, Y. Jiang, R. Zhou, and Jing Feng, Pressure dependence of electronic structure and superconductivity of the MnX (X= N, P, As, Sb). Sci. Rep. **6**, 21821 (2016).

[2] O. Rader, A. Kimura, N. Kamakura, K.-S. An, A. Kakizaki, S. Miyanishi, H. Akinaga, M. Shirai, K. Shimada, and A. Fujimori, Exchange splittings of Mn- and Sb-derived states by spin-resolved valence-band photoemission of MnSb. Phys. Rev. B **57**, R689–R692 (1998).

[3] A. Continenza, S. Picozzi, W. T. Geng, and A. J. Freeman, Coordination and chemical effects on the structural, electronic, and magnetic properties in Mn pnictides. Phys. Rev. B **64** 085204 (2001).

[4] R. Masrour, E. K. Hlil, M. Hamedoun, A. Benyoussef, O. Mounkachi and H. E. Moussaoui, Electronic and Magnetic Properties of MnSb Compounds. J. Supercon. Novel Magn. **28**, 1815-1819 (2015).

[5] L.N. Oveshnikov, A.B. Granovsky, A.B. Davydov, A.V. Bogach, A.M. Kharlamova, A.I. Ril',

B.A. Aronzon, Magnetic and magnetotransport properties of MnSb polycrystals near equatomic composition. J. Magn. Magn. Mater **563**, 169873 (2022).

[6] S. F. Marenkin, A. V. Kochura, A. D. Izotov, M. G. Vasil'ev, Manganese Pnictides MnP, MnAs, and MnSb are Ferromagnetic Semimetals: Preparation, Structure, and Properties (a Survey). Russ. J. Inorg. Chem., **63(14)**, 1753–1763 (2018).

[7] Y. Choi, P. J. Ryan, M. A. McGuire, B. C. Sales, J.-W. Kim, Giant magnetostriction effect near onset of spin reorientation in MnBi. Appl. Phys. Lett. **112** 192411 (2018).

[8] A. E. Taylor, T. Berlijn, S. E. Hahn, A. F. May, T. J. Williams, L. Poudel, S. Calder, R. S. Fishman, M. B. Stone, A. A. Aczel, H. B. Cao, M. D. Lumsden, and A. D. Christianson. Influence of interstitial Mn on magnetism in the room-temperature ferromagnet $Mn_{1+\delta}Sb$. Phys. Rev. B **91**, 224418 (2015).

[9] Y. He, S. Schneider, T. Helm, J. Gayles, D. Wolf, I. Soldatov, H. Borrmann, W. Schnelle, Rudolf Schaefer, G. H. Fecher, B. Rellinghaus and C. Felser, Topological Hall effect arising from the mesoscopic and microscopic non-coplanar magnetic structure in MnBi. Acta Materialia **226**, 117619 (2022).

[10] Y. He, J. Gayles, M. Yao, T. Helm, T. Reimann, V. N. Strocov, W. chnelle, M. Nicklas, Y. Sun, G. H. Fecher, and Claudia Felser, Large linear non-saturating magnetoresistance and high mobility in Ferromagnetic MnBi. Nat. Commun. **12**, 4576 (2021).

[11] M. S. Alam, A. Fakhredine, M. Ahmad, P. K. Tanwar, H.-Y. Yang, F. Tafti, G. Cuono, R. Islam, B. Singh, A. Lynnyk, C. Autieri, and M. Matusiak, Sign change of anomalous Hall effect and anomalous Nernst effect in the Weyl semimetal CeAlSi. Phys. Rev. B **107**, 085102 (2023).

[12] J. Mukherjee, T. S. Suraj, H. Basumatary, K. Sethupathi, and K. V. Raman, Sign reversal of anomalous Hall conductivity and magnetoresistance in cubic noncollinear antiferromagnet Mn_3Pt thin films. Phys. Rev. Materials **5**, 014201 (2021).

[13] R. Ibarra, E. Lesne, B. Sabir, J. Gayles, C. Felser, A. Markou, Anomalous Hall Effect in Epitaxial Thin Films of the Hexagonal Heusler MnPtGa Noncollinear Hard Magnet. Adv. Mater. Interfaces **9**, 2201562 (2022).

[14] P. K. Muduli, T. Higo, T. Nishikawa, D. Qu, H. Isshiki, K. Kondou, D. Nishio-Hamane, S. Nakatsuji, and YoshiChika Otani, Evaluation of spin diffusion length and spin Hall angle of the antiferromagnetic Weyl semimetal Mn_3Sn. Phys. Rev. B **99**, 184425 (2019).

[15] D. J. Groenendijk, C. Autieri, T. C. Van Thiel, W. Brzezicki, J. R. Hortensius, D. Afanasiev, N. Gauquelin, P. Barone, K. H. W. Van Den Bos, S. Van Aert, J. Verbeeck, A. Filippetti, S. Picozzi, M. Cuoco, and A. D. Caviglia, Berry phase engineering at oxide interfaces, Phys. Rev. Res. **2**, 023404 (2020).

[16] T. C. Van Thiel, W. Brzezicki, C. Autieri, J. R. Hortensius, D. Afanasiev, N. Gauquelin, D. Jannis, N. Janssen, D. J. Groenendijk, J. Fatermans, S. Van Aert, J. Verbeeck, M. Cuoco, and A. D. Caviglia, Coupling Charge and Topological Reconstructions at Polar Oxide Interfaces, Phys. Rev. Lett. **127**, 127202 (2021)

[17] R. D. dos Reis, M. Ghorbani Zavareh, M. O. Ajeesh, L. O. Kutelak, A. S. Sukhanov, Sanjay Singh, J. Noky, Y. Sun, J. E. Fischer, K. Manna, C. Felser, and M. Nicklas, Pressure tuning of the anomalous Hall effect in the chiral antiferromagnet Mn_3Ge, Phys. Rev. Materials **4**, 051401 (2020).

[18] C. Helman, A. Camjayi, E. Islam, M. Akabori, L. Thevenard, C. Gourdon, and M. Tortarolo, Anomalous Hall effect in MnAs: Intrinsic contribution due to Berry curvature, Phys. Rev. B **103**, 134408 (2021).

[19] J. L. Ma, H. L. Wang, X. L. Wang, and J. H. Zhao, Experimental evidence for an anisotropic Berry-phase effect on the anomalous Hall effect in MnAs films, Phys. Rev. B **97**, 064402 (2018).

[20] S. Singh, B. Dutta, S. W. D'Souza, M. G. Zavareh, P. Devi, A. S. Gibbs, T. Hickel, S. Chadov, C. Felser, and D. Pandey, Robust Bain distortion in the premartensite phase of a platinum-substituted Ni_2MnGa magnetic shape memory alloy. Nat Commun **8**, 1006 (2017).

[21] S. Singh, R. Rawat, S. E. Muthu, S. W. D'Souza, E. Suard, A. Senyshyn, S. Banik, P. Rajput, S. Bhardwaj, A. M. Awasthi, R. Ranjan, S. Arumugam, D. L. Schlagel, T. A. Lograsso, A. Chakrabarti, and S. R. Barman, Spin-Valve-Like Magnetoresistance in Mn_2NiGa at Room Temperature. Phys. Rev. Lett. **109**, 246601 (2012).

[22] P. Giannozzi, S. Baroni, N. Bonini, M. Calandra, R. Car, C. Cavazzoni, D. Ceresoli,. G. L. Chiarotti, M. Cococcioni, I. Dabo, A. D. Corso, S. de Gironcoli, S. Fabris, G. Fratesi, R. Gebauer, U. Gerstmann, C. Gougoussis,A. Kokalj, M. Lazzeri, L. Martin-Samos, N. Marzari, F. Mauri, R. Mazzarello, S. Paolini, A. Pasquarello, L. Paulatto, C. Sbraccia, S. Scandolo, G. Sclauzero, A. P.Seitsonen, A. Smogunov, P. Umari, and R. M. Wentzcovitch, QUANTUM ESPRESSO: a modular and open-source software project for quantum simulations of materials. J. Phys. Cond. Matt. **21**, 395502 (2009).

[23] J. P. Perdew, K. Burke, and M. Ernzerhof, Generalized Gradient Approximation Made Simple. Phys. Rev. Lett. **77**, 3865 (1996).

[24] D. R. Hamann, Optimized norm-conserving Vanderbilt pseudopotentials. Phys. Rev. B **88**, 085117 (2013).

[25] N. Marzari and D. Vanderbilt, Maximally localized generalized Wannier functions for composite energy bands. Phys. Rev. B **56**, 12847(1997).

[26] I. Souza, N. Marzari, and D. Vanderbilt, Maximally localized Wannier functions for entangled energy bands. Phys. Rev. B **65**, 035109 (2001).

[27] G. Pizzi, V. Vitale, R. Arita, S. Blügel, F. Freimuth, G. Géranton, M. Gibertini, D. Gresch, C. Johnson, T. Koretsune, J. I.-Azpiroz, H. Lee, J.-M. Lihm, D. Marchand, A. Marrazzo, Y. Mokrousov, J. I. Mustafa, Y. Nohara, Y. Nomura, L. Paulatto, S. Poncé, T. Ponweiser, J. Qiao, F. Thöle, S. S. Tsirkin, M. Wierzbowska, N. Marzari, D. Vanderbilt, I. Souza, A. A. Mostofi, and J. R. Yates, Wannier90 as a community code: new features and applications. J. Phys. Cond. Matt. **32**, 165902 (2020).

[28] P. Singh, Structure and growth of MnSb and MnBi thin films. **7(7)**, 293–298 (1988).

[29] P. Radhakrishna and J. W. Cable, Inelastic-neutron-scattering studies of spin-wave excitations in the pnictides MnSb and CrSb. Phys. Rev. B **54**, 11940 (1996).

[30] J. Rodríguez-Carvajal, FULLPROF, a Rietveld and pattern matching and analysis programs version 2016, Laboratoire Leon Brillouin, CEA-CNRS, France, http://www.ill.eu/sites/ fullprof/

[31] K. Momma and F. Izumi, VESTA 3 for three-dimensional visualization of crystal, volumetric and morphology data, J. Appl. Crystallogr. **44**, 1272-1276 (2011).

[32] W. Reimers, E. Hellner, W. Treutmann, G. Heger, Magnetic phase diagram of the system $Mn_{1-x}Cr_xSb$ ($0 \leq x \leq 1$). Journal of Physics C: Solid State Physics, **15(16)**, 3597–3615 (1982).

[33] G. Z. Xu, Y. Du, X. M. Zhang, H. G. Zhang, E. K. Liu, W. H. Wang, and G. H. Wu, Magneto-transport properties of oriented Mn2CoAl films sputtered on thermally oxidized Si substrates. Appl. Phys. Lett. **104**, 242408 (2014).

[34] R. Podloucky, Electronic structure of MnSb. Sol. State Commun. **50**, 763–767 (1984).

[35] H. Ido, Magnetic properties of mixed crystals with NiAs-type structure. J. Appl. Phys. **57**, 3247 (1985).

[36] X. H. Chen, C. H. Wang, G. Y. Wang, X. G. Luo, J. L. Luo, G. T. Liu, and N. L. Wang, Thermal hysteresis and anisotropy in the magnetoresistance of antiferromagnetic $Nd_{2-x}Ce_xCuO_4$. Phys. Rev. B **72**, 064517 (2005).

[37] P. Sarkar, P. Mandal, K. Mydeen, A. K. Bera, S. M. Yusuf, S. Arumugam, C. Q. Jin, T. Ishida, and S. Noguchi, Role of external and internal perturbations on the ferromagnetic phase transition in $Sm_{0.52}Sr_{0.48}MnO_3$. Phys. Rev. B **79**, 144431 (2009).

[38] J.A.M Santos, J.F Collingwood, J.B Sousa, S.B Palmer, Anomalous magnetoresistance near the spin reorientation transition of dilute Gd–Y single crystals, J. Magn. Magn. Mater., **272–276**, E491-E492 (2004).

[39] H. Li, B. Ding, J. Chen, Z. Li, Z. Hou, E. Liu, H. Zhang, X. Xi, G. Wu, W. Wang, Large topological Hall effect in a geometrically frustrated kagome magnet Fe_3Sn_2. Appl. Phys. Lett. **114** (19) 192408 (2019).

[40] Q. Wang, S. Sun, X. Zhang, F. Pang, and H. Lei, Anomalous Hall effect in a ferromagnetic Fe_3Sn_2 single crystal with a geometrically frustrated Fe bilayer kagome lattice. Phy. Rev. B **94**, 075135 (2016).

[41] A. L. Balk, F. Li, I. Gilbert, J. Unguris, N. A. Sinitsyn, and S. A. Crooker, Broadband

Spectroscopy of Thermodynamic Magnetization Fluctuations through a Ferromagnetic Spin-Reorientation Transition. Phys. Rev. X **8**, 031078 (2018).

[42] C. M. Hurd, The Hall Effect in Metals and Alloys (Plenum, New York, 1972).

[43] T. Kida, L. A. Fenner, A. A. Dee, I. Terasaki, M. Hagiwara, and A. S. Wills, The giant anomalous Hall effect in the ferromagnet Fe3Sn2—a frustrated kagome metal. J. Phys.: Condens. Matter. **23** 112205 (2011).

[44] G. K. Shukla, J. Sau, N. Shahi , A. K. Singh, M. Kumar, and S. Singh, Anomalous Hall effect from gapped nodal line in the Co_2FeGe Heusler compound. Phys. Rev. B **104**, 195108 (2021).

[45] K. Manna, L. Muechler, T. H. Kao, R. Stinshoff, Y. Zhang, J. Gooth, N. Kumar, G. Kreiner, K. Koepernik, and R. Car, J. Kübler, G. H. Fecher, C. Shekhar, Y. Sun, and C. Felser, From Colossal to Zero: Controlling the Anomalous Hall Effect in Magnetic Heusler Compounds via Berry Curvature Design. Phys. Rev. X **8**, 041045 (2018).

[46] B. K. Hazra, M. M. Raja, R. Rawat, A. Lakhani, S. Kaul, and S. Srinath, J. Magn. Magn. Mater. Effect of disorder on the anomalous Hall conductivity of Co_2FeSi thin films. **448**, 371 (2018).

[47] Y. Tian, L. Ye, and X. Jin, Proper Scaling of the Anomalous Hall Effect. Phys. Rev. Lett. **103**, 087206 (2009).

[48] D. Hou, G. Su, Y. Tian, X. Jin, S. A. Yang, and Q. Niu, Multivariable Scaling for the Anomalous Hall Effect. Phys. Rev. Lett. **114**, 217203 (2015).

[49] N. Shahi, A. K. Jena, G. K. Shukla, V. Kumar, S. Rastogi, K. K. Dubey, I. Rajput, S. Baral, A. Lakhani, S.-C. Lee, S. Bhattacharjee, and S. Singh, Antisite disorder and Berry curvature driven anomalous Hall effect in the spin gapless semiconducting Mn_2CoAl Heusler compound. Phys. Rev. B **106**, 245137 (2022).

[50] G. K. Shukla, A. K. Jena, N. Shahi, K. K. Dubey, I. Rajput, S. Baral, K. Yadav, K. Mukherjee, A. Lakhani, K. Carva, S.-C. Lee, S. Bhattacharjee, S. Singh, Atomic disorder and Berry phase driven anomalous Hall effect in a Co_2FeAl Heusler compound. Phys. Rev. B **105**, 035124 (2022).

[51] G. K. Shukla, J. Sau, V. Kumar, M. Kumar, and S. Singh, Band splitting induced Berry flux

and intrinsic anomalous Hall conductivity in the NiCoMnGa quaternary Heusler compound. Phys. Rev. B **106**, 045131 (2022).

[52] L. Zhu, D. Pan, J. Zhao, Anomalous Hall effect in epitaxial L1-$Mn_{1.5}Ga$ films with variable chemical ordering. Phys. Rev. B **89**, 220406 (2014).

[53] A. Crpéieux and P. Bruno, Theory of the anomalous Hall effect from the Kubo formula and the Dirac equation, Phys. Rev. B **64**, 014416 (2001)

[54] S.-Y. Yang, Y. Wang, B. R. Ortiz, D. Liu, J. Gayles, E. Derunova, R. G.-Hernandez, L. šmejkal, Y. Chen, S. S. P. Parkin, S. D. Wilson, E. S. Toberer, T. McQueen, and M. N. Ali, Giant unconventional anomalous Hall effect in the metallic frustrated magnet candidate, KV_3Sb_5. Sci. Adv. **6**, eabb6003 (2020).

[55] J. Shen, Q. Yao, Q. Zeng, H. Sun, X. Xi, G. Wu, W. Wang, B. Shen, Q. Liu, E. Liu, Local Disorder-Induced Elevation of Intrinsic Anomalous Hall Conductance in an Electron-Doped Magnetic Weyl Semimetal. Phys. Rev. Lett. **125**, 086602 (2020).

[56] J. Shen, S. Zhang, T. Liang, J. Wang, Q. Zeng, Y. Wang, H. Wei, E. Liu, X. Xu, Intrinsically enhanced anomalous Hall conductivity and Hall angle in Sb-doped magnetic Weyl semimetal $Co_3Sn_2S_2$. APL Mater. **10**, 090705 (2022).

[57] P. Nozieres and C. Lewiner, A simple theory of the anomalous hall effect in semiconductors. Journal de Physique **34**, 901 (1973).

[58] S. Onoda, N. Sugimoto, and N. Nagaosa, Intrinsic versus extrinsic anomalous Hall efect in ferromagnets. Phys. Rev. Lett. **97**, 126602 (2006).

[59] E. Liu, Y. Sun, N. Kumar, L. Muechler, A. Sun, L. Jiao,S. Y. Yang, D. Liu, A. Liang, Q. Xu, J. Kroder, V. Süß, H. Borrmann, C. Shekhar, Z. Wang, C. Xi, W. Wang, W.Schnelle, S. Wirth, Y. Chen, S. T. B. Goennenwein, and C. Felser, Giant anomalous Hall effect in a ferromagnetic kagome-lattice semimetal. Nat. Phys. **14**, 1125–1131 (2018).

[60] H. Siddiquee, C. Broyles, E. Kotta, S. Liu, S. Peng, T. Kong, B. Kang, Q. Zhu, Y. Lee, L. Ke, H. Weng, J. D. Denlinger, L. A. Wray, and S. Ran, Breakdown of the scaling relation of anomalous Hall effect in Kondo lattice ferromagnet USbTe. Nat. Commun. **14**, 527 (2023).

[61] F. H. Yu, T. Wu, Z. Y. Wang, B. Lei, W. Z. Zhuo, J. J. Ying, and X. H. Chen, Concurrence of anomalous Hall effect and charge density wave in a superconducting topological kagome metal. Phys. Rev. B **104**, L041103 (2021).

[62] M. Gradhand, D. V. Fedorov, F. Pientka, P. Zahn, I. Mertig, and B. L. Györffy, First-principle calculations of the Berry curvature of Bloch states for charge and spin transport of electrons, J. Phys.: Condens. Matter. **24**, 213202 (2012).

[63] A. K. Nayak, J. E. Fischer, Y. Sun, B. Yan, J. Karel, A. C. Komarek, C. Shekhar, N. Kumar, W. Schnelle, J. Kübler, C. Felser, and S. S. P. Parkin, Large anomalous Hall effect driven by a nonvanishing Berry curvature in the noncolinear antiferromagnet Mn_3Ge. Sci. Adv. **2**, e1501870 (2016).

[64] S. Nakatsuji, N. Kiyohara, and T. Higo, Large anomalous Hall efect in a non-collinear antiferromagnet at room temperature. Nature **527**, 212–215 (2015).

[65] N. Kanazawa, Y. Onose, T. Arima, D. Okuyama, K. Ohoyama, S. Wakimoto, K. Kakurai, S. Ishiwata, and Y. Tokura, Large Topological Hall Effect in a Short-Period Helimagnet MnGe. Phys. Rev. Lett. **106**, 156603 (2011).

[66] B. Giri, A. I. Mallick, C. Singh, P. V. P. Madduri, F. Damay, A. Alam, and A. K. Nayak, Robust topological Hall effect driven by tunable noncoplanar magnetic state in Mn-Pt-In inverse tetragonal Heusler alloys. Phys. Rev. B **102**, 014449 (2020).

[67] Z. H. Liu, Y. J. Zhang, G. D. Liu, B. Ding, E. K. Liu, H. M. Jafri, Z. P. Hou, W. H. Wang, X. Q. Ma, and G. H. Wu, Transition from Anomalous Hall Effect to Topological Hall Effect in Hexagonal Non-Collinear Magnet Mn_3Ga. Sci Rep **7**, 515 (2017).

[68] C. Sürgers, G. Fischer, P. Winkel, and H. v. Löhneysen, Large topological Hall effect in the non-collinear phase of an antiferromagnet. Nat. Commun. **5**, 3400 (2014).

[69] N. J. Ghimire, R. L. Dally, L. Poudel, D. C. Jones, D. Michel, N. T. Magar, M. Bleuel, M. A. McGuire, J. S. Jiang, J. F. Mitchell, J. W. Lynn and I. I. Mazin, Competing magnetic phases and fluctuation-driven scalar spin chirality in the kagome metal YMn_6Sn_6. Sci. Adv. **6**, eabe2680 (2020).

[70] J. Liu, S. Zuo, X. Zheng, Y. Zhang, T. Zhao, F. Hu, J. Sun, B. Shen, Magnetic transition behavior and large topological Hall effect in hexagonal $Mn_{2-x}Fe_{1+x}Sn$ (x=0.1) magnet. Appl. Phys. Lett. **117**, 052407 (2020).

[71] Y. Shiomi, M. Mochizuki, Y. Kaneko, and Y. Tokura, Hall Effect of Spin-Chirality Origin in a Triangular-Lattice Helimagnet $Fe_{1.3}Sb$. Phys. Rev. Lett. **108**, 056601 (2012).

[72] M. J. Donahue, D. G. Porter, OOMMF User's Guide, Version 1.0, Integracy Report NISTIR 6376, National Institute of Standards and Technology, Gaithersburg, MD, (Sept 1999).

[73] P. K. Sivakumar, B. Göbel, E. Lesne, A. Markou, J. Gidugu, J. M. Taylor, H. Deniz, J. Jena, C. Felser, I. Mertig, and S. S. P. Parkin, Topological Hall Signatures of Two Chiral Spin Textures Hosted in a Single Tetragonal Inverse Heusler Thin Film. ACS Nano. **14**(10), 13463-13469 (2020).

[74] W. Wang, Y. F. Zhao, F. Wang, M. W. Daniels, C. Z. Chang, J. Zang, D. Xiao, and W. Wu, Chiral-Bubble-Induced Topological Hall Effect in Ferromagnetic Topological Insulator Heterostructures. Nano Lett. **21**(2), 1108-1114 (2021).

[75] D. Chakrabartty, S. Jamaluddin, S.K. Manna, A. K. Nayak, Tunable room temperature magnetic skyrmions in centrosymmetric kagome magnet Mn_4Ga_2Sn. Commun. Phys. **5**, 189 (2022).

[76] J. Liu, S. Zuo, H. Li, Y. Liu, X. Zheng, Y. Zhang, T. Zhao, F. Hu, J. Sun, and B. Shen, Spontaneous magnetic bubbles and large topological Hall effect in $Mn_{3-x}Fe_xSn$ compound. Scr. Mater., **187**, 268-273 (2020).